Applied Surface Science 280 (2013) 967–974

Contents lists available at SciVerse ScienceDirect

Applied Surface Science

journal homepage: www.elsevier.com/locate/apsusc

A facile modification of g-C_3N_4 with enhanced photocatalytic activity for degradation of methylene blue

Fei Chang[a,*], Yunchao Xie[a], Chenlu Li[a], Juan Chen[a], Jieru Luo[a], Xuefeng Hu[b,**], Jiaowen Shen[c]

[a] School of Environment and Architecture, University of Shanghai for Science and Technology, Shanghai 200093, PR China
[b] Key Laboratory of Coastal Zone Environmental Processes and Ecological Remediation, Yantai Institute of Coastal Zone Research, Chinese Academy of Sciences, Yantai, Shandong 264003, PR China
[c] School of Urban Development and Environmental Engineering, Shanghai Second Polytechnic University, Shanghai 201209, PR China

ARTICLE INFO

Article history:
Received 21 March 2013
Received in revised form 22 May 2013
Accepted 25 May 2013
Available online 3 June 2013

Keywords:
Graphitic carbon nitride
Sodium nitrate
Photocatalysis
Methylene blue

ABSTRACT

In this investigation, a facile modification of g-C_3N_4 through co-pyrolysis of melamine and sodium nitrate or potassium nitrate was reported and the as-synthesized samples were characterized by a collection of techniques, such as X-ray diffraction, scanning electron microscopy, transmission electron microscopy, UV–vis diffuse reflectance spectroscopy, nitrogen adsorption–desorption, X-ray photoelectron spectroscopy, Fourier transform infrared spectroscopy, and elemental analysis. Based upon the analysis, we speculated that the g-C_3N_4 framework was partially destroyed to produce cyano-containing fragments, which resulted into the variation of physical and optical properties, further affecting the adsorption and photocatalytic performance of g-C_3N_4 on the dye methylene blue. Furthermore, we found that nitrate anions rather than sodium or potassium ions had important effect on the structure and photocatalytic performance of g-C_3N_4. In addition, the photocatalysis mechanism and reusability test were also investigated and discussed in the study.

1. Introduction

Semiconductor photocatalyts have attracted much attention due to its potential employments in organic and inorganic pollutants remediation in wastewater in the last decade [1,2]. Among numerous semiconductors reported, TiO_2 is the most widely researched one because of its excellent photochemical stability, nontoxicity, and high photocatalytic capability [3,4]. However, TiO_2 is able to drive the photocatalysis through excitement by only the ultraviolet light ($\lambda < 400$ nm), accounting for about 4% of the sunlight, which greatly limits its practical applications [5]. Consequently, much effort has been made on the development of photocatalytic processes that efficiently utilized the visible light, including modification of TiO_2 with metals [6], non-metals [7], semiconductor oxides [8], and photo-sensitizers [9], or development of new type photocatalysts with high activity under a wide range of visible light [10,11].

Most recently, polymeric graphitic carbon nitride (g-C_3N_4), regarded as the most stable phase of covalent carbon nitride solids under ambient conditions, has been of great concern of a favorable photocatalyst because of the unique features, such as special electronic and optical structure, and high chemical and thermal stability [12,13]. Wang et al. firstly reported that g-C_3N_4 showed a good photocatalytic performance for hydrogen or oxygen evolution *via* splitting water under visible-light illumination in the presence of sacrificial reagents [12]. Zou et al. confirmed that the metal-free g-C_3N_4 had excellent performance on the photooxidation of organic pollutants under visible light irradiation [14]. However, the photocatalytic efficiency of bare g-C_3N_4 was relatively low and far from satisfactory. Several strategies have thus been adopted to enhance the photocatalytic performance of g-C_3N_4, including designing an appropriate textural porosity [15,16], doping with metal oxides or nonmetal elements [17–19], and exfoliation of bulk phase to nanosheets [20–23]. Though a lot of efforts have been exerted to prepare structurally new g-C_3N_4 compounds, it is still a big challenge to manufacture g-C_3N_4 materials with enhanced visible-light photocatalytic performance.

In this study, we have successfully prepared the g-C_3N_4 samples *via* co-pyrolysis of melamine and sodium nitrate or potassium nitrate. It was reported that sodium nitrate could decompose to nitrogen oxides and gaseous oxygen over 500 °C [24]. The resultant nitrogen oxides might attack the tri-*s*-triazine at high temperature as oxidants to alter the framework of g-C_3N_4. The crystallinity,

* Corresponding author. Tel.: +86 21 55271722.
** Corresponding author. Tel.: +86 535 2109157.
E-mail addresses: feichang@usst.edu.cn (F. Chang), xfhu@yic.ac.cn (X. Hu).

0169-4332/$ – see front matter © 2013 Elsevier B.V. All rights reserved.
http://dx.doi.org/10.1016/j.apsusc.2013.05.127

phase, morphology, specific surface area, and optical property of the samples were fully investigated. The photocatalytic activities of the as-prepared samples were estimated by treating methylene blue (MB) aqueous under visible light illumination ($\lambda > 420$ nm). The g-C_3N_4 synthesized in the presence of sodium nitrate showed high removal performance in comparison to pure g-C_3N_4 sample. The enhancement of photocatalytic activity could be attributed to a synergistic effect, including the strong adsorption of MB, and low band gap energy. The photocatalysis mechanism and reusability test were also investigated and discussed systematically.

2. Materials and methods

2.1. Reagents

Melamine ($C_3H_6N_3$, 99%), sodium nitrate ($NaNO_3$, AR), potassium nitrate (KNO_3, AR), methylene blue (MB, AR), *tert*-butyl alcohol (TBA, AR), disodium ethylenediaminetetraacetate dihydrate (EDTA-2Na, AR), terephthalic acid (TA, AR), and other chemicals involved were purchased from Sinopharm Chemical Reagent Co., Ltd. (China) and used directly for the experiment without any further purification. All aqueous solutions were prepared with the deionized water.

2.2. Preparation of modified g-C_3N_4 samples

In the experimental, co-pyrolysis of melamine together with $NaNO_3$ was employed to synthesize modified g-C_3N_4 in a semi-closed system. Typically, different molar ratios of melamine and $NaNO_3$ were mixed and ground to fine powders using a mortar and a pestle. Then the finely ground powders were charged into a covered ceramics crucible and heated at 500 °C in a muffle furnace for 2 h and at 550 °C for another 2 h for the sake of further deammonation. The sample was allowed to cool to room temperature before removal from muffle furnace. The resultant powders were washed with dilute hydrochloric acid, absolute ethanol, deionized water, and acetone to remove any soluble impurities, and dried overnight at 100 °C in an oven to obtain target samples, denoting as g-C_3N_4-S$_x$, where S and subscript x (3, 5, 10, 20, 30) referred to $NaNO_3$ and molar ratios of melamine to $NaNO_3$, respectively. The co-pyrolysis of melamine with KNO_3 was conducted using a same protocol and corresponding compounds were denoted as g-C_3N_4-P$_x$. Pure g-C_3N_4 was also synthesized as a reference from melamine polycondensation under the identical condition, as reported [14].

2.3. Characterization

X-ray diffraction (XRD) patterns were recorded on a Bruker D8 Advance X-ray diffractometer using Cu Kα radiation source ($\lambda = 1.05406$ Å). The accelerating voltage and the applied current were 40 kV and 80 mA. The scanning electron micrographs (SEM) were taken on a Philips XL-30 electron microscope. The transmission electron microscopy (TEM) measurements were conducted on a JEOL JEM-2011electron microscope with acceleration voltage of 200 kV. The specific surface areas of samples were measured by N_2 sorption at the liquid-nitrogen temperature of 77 K using an automatic surface area and size analyzer (3H-2000PS2). All samples were degassed at 473 K for 2 h prior to measurements. X-ray photoelectron spectroscopy (XPS) measurements were performed using a RBD upgraded PHI 5000 C ESCA System (Perkin Elmer) with Mg Kα (1253.6 eV) radiation. Thermal stability and phase transformation were carried out by using the thermogravimetric-differential scanning calorimetry analysis (TG-DSC, STA-449C). The detected temperature range was from room temperature to 800 °C at a heating rate of 10 °C min^{-1}. UV–vis diffuse reflectance spectra (UV–vis DRS) were obtained on a UV–vis spectrophotometer (Hitachi U-4100) with $BaSO_4$ as a reflectance standard. Fourier transform infrared spectroscopy (FT-IR) was operated on a Bruker V-70 Fourier transform-infrared spectrophotometer using a KBr pellet technique. Elemental analysis (EA) was carried out on an Elemental Vario III elemental analyzer. Surface electrical property was evaluated on a zeta potential analyzer (Malvern Zetasizer NANO ZS).

2.4. Photocatalytic measurements

Photocatalytic measurements were carried out by decomposing dye MB in aqueous solution using a LIMX-VII apparatus manufactured by Bylabo Precision Instrument Co. Ltd. (Xi'an, China). A 400 W halogen lamp (Institute for Electric Light Sources, Beijing) with 420 nm cutoff filters was used as a light source to provide visible light irradiation. An aqueous solution of MB (20 mgL^{-1}, 40 mL) containing photocatalyst powder (80 mg) was magnetically stirred in the dark for 2 h to achieve the adsorption–desorption equilibrium between MB molecules and photocatalyst. During irradiation, 3.5 mL aliquots were sampled at fixed time intervals, diluted, and centrifuged to remove suspended photocatalyst powders. The supernatant solution was analyzed by a UV–vis spectrophotometer (Purkinje General T6) at the maximum absorption band 664 nm.

The catalyst durability was estimated according to the procedure below: after each run, the catalyst was collected from aqueous solution by centrifugation, washed with deionized water and ethanol for several times, and dried overnight at 100 °C. Afterwards, each recycling test was performed under same conditions.

The effects of various active species on the degradation of MB were examined to understand the photocatalytic mechanism. Typically, a certain amount of photocatalyst with EDTA-2Na (10 mM, a quencher of h^+) or TBA (10% by volume, a quencher of •OH) was dispersed in MB solution (40 mL, 20 mgL^{-1}). The method was similar to the former photocatalytic measurements.

The detection of hydroxyl radicals amount (•OH) was conducted according to the literature [17]. The fluorescence spectra of generated 2-hydroxy terephthalic acid (TAOH) were measured on a Shimadzu RF-5301PC spectrofluorophotometer with the employed excitation light 320 nm.

3. Results and discussion

3.1. XRD patterns

Fig. 1 shows X-ray diffraction patterns for all as-synthesized samples. It is well known that the g-C_3N_4 is constructed based on tri-*s*-triazine building blocks. The high-intensity peak at around 27.7° is a characteristic (0 0 2) interlayer stacking reflection of conjugated aromatic segments. The calculated interlayer distance of aromatic units ($d = 0.325$ nm) is relatively smaller than that of the crystalline g-C_3N_4 ($d = 0.34$ nm) [14]. The small peak at nearly 13.2°, indexed as (1 0 0), is relevant to the in-plane structural repeating motif, like the hole-to-hole distance of the continuous tri-*s*-triazine pores [25,26]. The presence of both well-resolved diffraction peaks identifies the formation of graphite C_3N_4 framework. Comparing with the pure g-C_3N_4, the (1 0 0) diffraction peak of g-C_3N_4-S$_x$ becomes gradually decrease with the increase of $NaNO_3$ amount and completely disappears when molar ratio of melamine to $NaNO_3$ is beyond 5:1. It might presumably be attributed to that the presence of $NaNO_3$ could partially destroy the graphitic structure to produce some fragments, and thus somewhat altered the in-plane structural repeating network [27]. The same phenomenon was also observed in g-C_3N_4-P$_x$ samples.

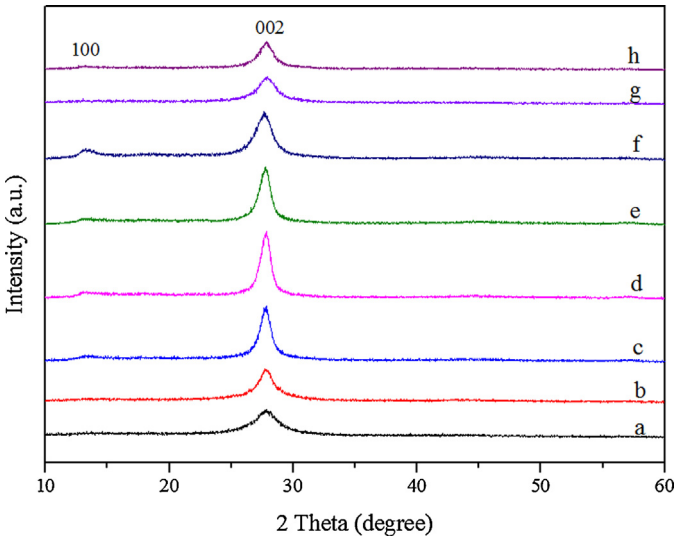

Fig. 1. XRD patterns of (a) g-C_3N_4-S_3; (b) g-C_3N_4-S_5; (c) g-C_3N_4-S_{10}; (d) g-C_3N_4-S_{20}; (e) g-C_3N_4-S_{30}; (f) g-C_3N_4; (g) g-C_3N_4-P_5; (h) g-C_3N_4-P_{10}.

3.2. FT-IR spectra

FT-IR spectra in Fig. 2 present a comparison of g-C_3N_4-S_x and g-C_3N_4-P_x series to pure g-C_3N_4 in chemical structure. The strong absorption band in the range of 1200–1650 cm^{-1} is assigned to the typical skeletal stretching vibrations of the *s*-triazine or tri-*s*-triazine and the sharp peak centered at 808 cm^{-1} is a characteristic breathing mode of the triazine units [28]. The broad adsorption band at 3100–3300 cm^{-1} is indexed to the stretching vibration modes of residual N—H components or the O—H bands, associating with uncondensed amino groups and absorbed H_2O molecules, respectively [29]. Interestingly, a small peak ranging from 2100 to 2200 cm^{-1} is found among the g-C_3N_4-S_x and g-C_3N_4-P_x series and enhances with the increase of $NaNO_3$ or KNO_3 amount, assigning to the presence of C≡N triple bonds [28,30]. It was reported that $NaNO_3$ started to decompose over 500 °C to generate molecular oxygen and nitrogen oxides [24]. The generated nitrogen oxides were suspected to role as oxidation reagents to attack and subsequently broke the tri-*s*-triazine units to produce C≡N moiety-containing fragments. The partial collapse of g-C_3N_4 framework

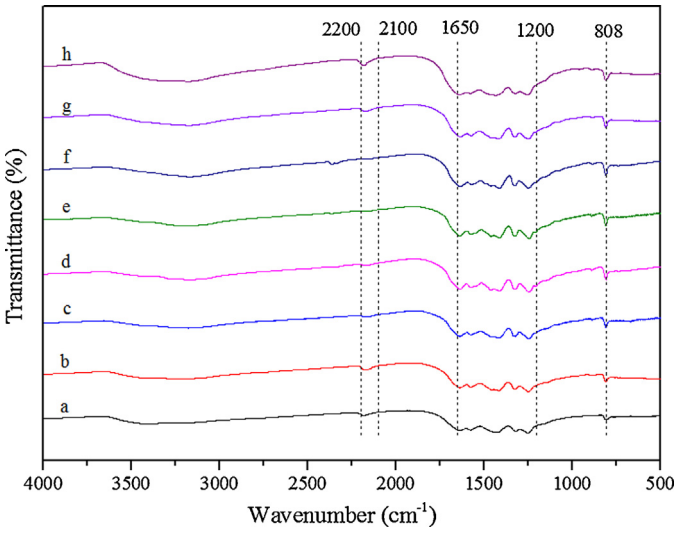

Fig. 2. FT-IR spectra of (a) g-C_3N_4-S_3; (b) g-C_3N_4-S_5; (c) g-C_3N_4-S_{10}; (d) g-C_3N_4-S_{20}; (e) g-C_3N_4-S_{30}; (f) g-C_3N_4; (g) g-C_3N_4-P_5; (h) g-C_3N_4-P_{10}.

was also proven by the decrease of intensity of the absorption band in a range of 1200–1650 cm^{-1} and the peak centered at 808 cm^{-1}, and the absence of (1 0 0) peak in XRD analysis as well. Similar results were found in Yue's report when they doped zinc species into g-C_3N_4 framework to prepare a metal-containing carbon nitride [27] and Wang's observation when they exfoliated the bulk g-C_3N_4 to nanosheets [23].

3.3. XPS analysis

X-ray photoelectron spectroscopy (XPS) was further utilized to investigate the chemical compositions and structural environments of the g-C_3N_4-S_5 and pure g-C_3N_4. In Fig. 3B and C, the XPS C 1s peaks and N 1s peaks of g-C_3N_4-S_5 and g-C_3N_4 are almost identical, revealing that the graphite carbon nitride framework was mainly retained after addition of $NaNO_3$, even some parts of framework were destroyed, identified by XRD and FT-IR analysis. The XPS C 1s can be deconvoluted into two components with binding energy of 284.6 eV (C1) and 287.6 eV (C2). The former peak centered at 284.6 eV is typically ascribed to graphitic carbon adsorbed to the surface. The last peak with binding energy of 287.6 eV corresponds to N=C—N groups of triazine rings [18]. In Fig. 3C, the XPS N 1s peaks are composed of three peaks centered at 398.1 eV (N1), 399.1 eV (N2), and 400.7 eV (N3). The N1 peak assigning to nitrogen sp^2-bonded to carbon demonstrates the presence of triazine rings, while both the N2 and N3 peaks are relevant to the presence of the C—N—H and C≡N bonding, respectively [31]. The O 1s signal in Fig. 3D is presumably due to the absorbed H_2O or CO_2 molecules on the samples surface [32], consisting with the above FT-IR analysis. Only three elements (C, N, O) can be observed in pure g-C_3N_4, however, a signal assigning to element sodium is found in the sample g-C_3N_4-S_5, as seen in Fig. 3A. Element potassium is also observed in Fig. A.1., though the signal is overlapped by C1s peak.

Supplementary material related to this article found, in the online version, at http://dx.doi.org/10.1016/j.apsusc.2013.05.127.

3.4. TG analysis

The thermal stability and phase transformation were carried out in an open system by using the thermogravimetric-differential scanning calorimetric analysis in Fig. 4. A slight weight loss is observable at the temperature 20–200 °C, owning to the removal of physically absorbed water [33]. In addition, the weight loss increases with the increase of $NaNO_3$ involved, especially g-C_3N_4-S_5 with a weight loss nearly 10%. Pure g-C_3N_4 becomes unstable when the heating temperature is above 400 °C, and heating to 650 °C results in no residue of the material being detectable. Similar phenomena are found for g-C_3N_4-S_x series, except some residues retained in g-C_3N_4-S_x series over 650 °C. TG-DSC analyses of g-C_3N_4-S_x were supplied in Fig. A.2–5. Moreover, the amount of residue retained, identified as sodium species in XPS description, increases along with the increase of $NaNO_3$ addition. It was understandable that some $NaNO_3$ might be coated by layers of melamine during grinding and these sodium species were residually retained after calcinations, even washed with deionized water and organic solvents for several times. Similarly, residue potassium species were also detectable from XPS spectra. In addition, we studied the effect of sodium or potassium species on the structure of formed g-C_3N_4 series. From Fig. A.6, XRD patterns of g-C_3N_4-S_5 and g-C_3N_4-P_5, and g-C_3N_4-S_{10} and g-C_3N_4-P_{10} are almost identical, respectively. However, XRD patterns of g-C_3N_4-S_5 or g-C_3N_4-P_5 are quite different from g-C_3N_4-S_{10} or g-C_3N_4-P_{10}. It indicated that amount of nitrate ions had crucial effect on the structure of g-C_3N_4 and sodium or potassium species only played roles of counter-ions, which was also proven in Fig. A.7.

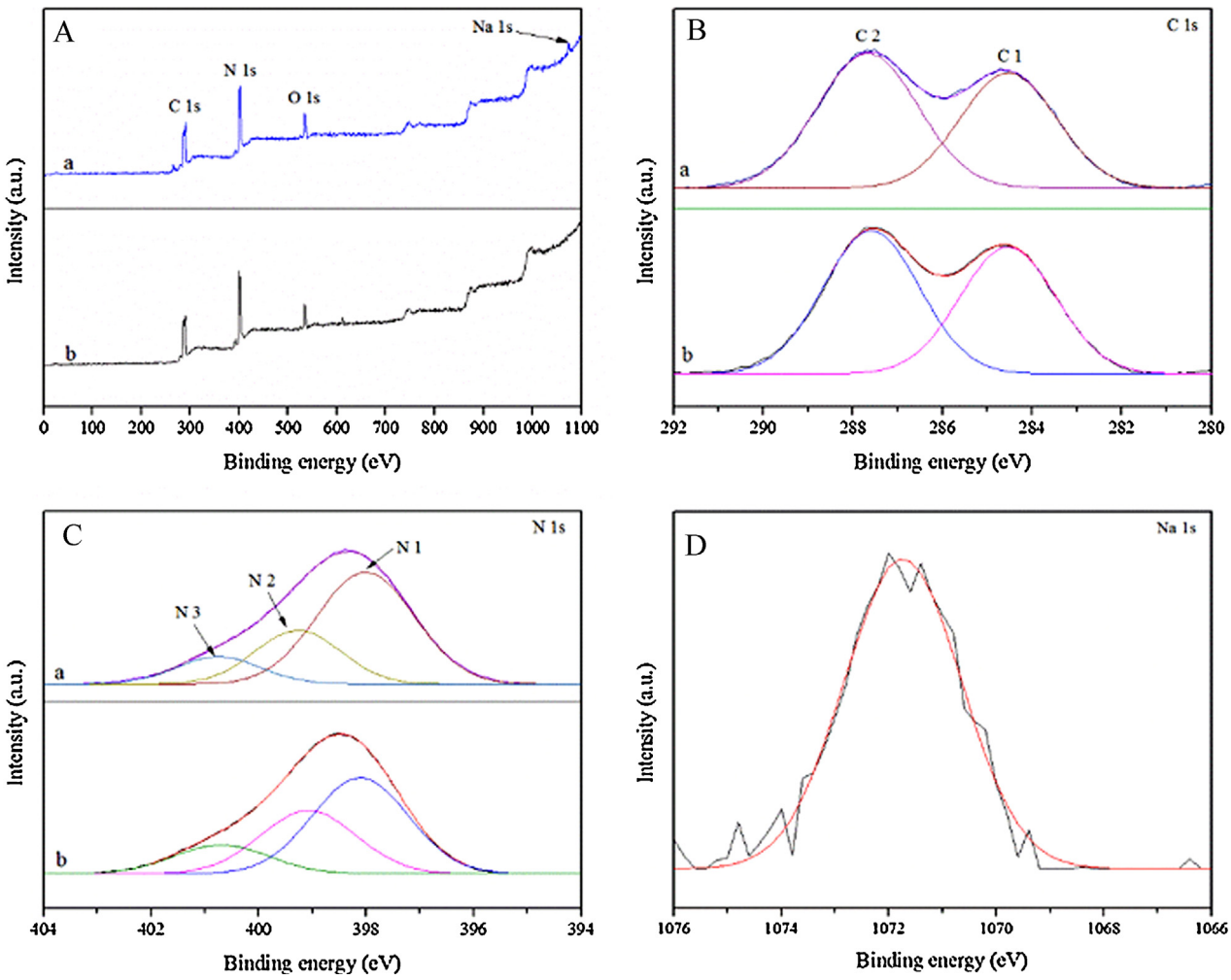

Fig. 3. XPS spectra (A) spectra, (B) C 1s, (C) N 1s for (a) g-C_3N_4-S_5 and (b) g-C_3N_4; (D) Na 1s for g-C_3N_4-S_5.

Supplementary material related to this article found, in the online version, at http://dx.doi.org/10.1016/j.apsusc.2013.05.127.

3.5. UV–vis diffuse reflectance spectroscopy

The optical property of the g-C_3N_4-S_x series and pure g-C_3N_4 were measured by UV–vis diffuse reflectance spectroscopy, as shown in Fig. 5. The adsorption edges and corresponding band gap energy of the as-synthesized samples are listed in Table 1. The adsorption edge of the pure g-C_3N_4 sample was estimated at approximately 454 nm and the corresponding band gap energy was calculated as 2.73 eV [12]. Thus, visible light ($\lambda > 420$ nm) irradiation was capable of exciting pure g-C_3N_4 to produce photoinduced electrons and holes, facilitating the photocatalytic reactions. Further observation indicated that all g-C_3N_4 samples prepared with the addition of $NaNO_3$ exhibited strong light absorption and obvious red shift of adsorption edge in comparison to pure g-C_3N_4. Red shift of adsorption edge and the increased light absorption meant more visible light harvesting and shrinkage of band gap energy meant the ease of producing photoinduced electrons and holes [34]. In addition, C/N atom ratios of g-C_3N_4-S_x series ranging 0.656 to 0.695 by elemental analysis were relatively large in comparison to that of pure g-C_3N_4. Based on the XRD and FT-IR analysis, partial destroy of continuous tri-*s*-triazine units after addition of $NaNO_3$ produced some cyano moiety-containing fragments, which were defects on the regular graphite framework. We attributed that the presence of these fragments was the main reason causing red shift of adsorption edge of modified g-C_3N_4 samples, the shrinkage of band gap, and increase of C/N atom ratios.

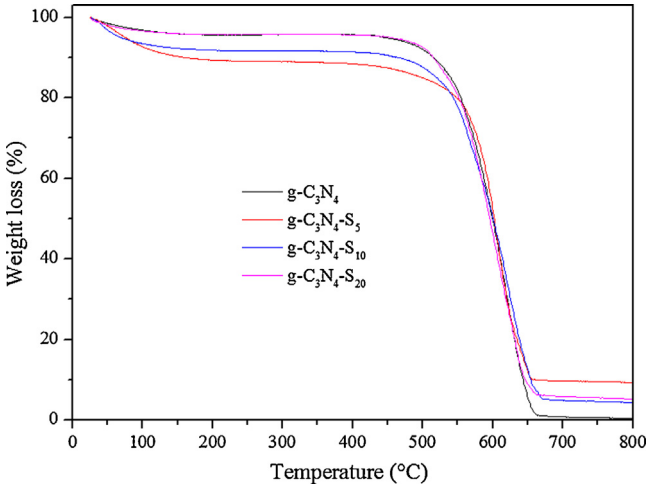

Fig. 4. TG thermograms of the as-prepared g-C_3N_4 samples.

Table 1
Chemical compositions, adsorption edges, band gaps, and specific surface areas of pure g-C_3N_4 and g-C_3N_4-S_x series.

Samples	C (at%)	N (at%)	C/N ratio	Adsorption edge (nm)	Band gap (E_g)	S_{BET} (g/m^2)
g-C_3N_4-S_3	33.9	61.0	0.648	453	2.74	2.78
g-C_3N_4-S_5	30.9	51.9	0.695	473	2.62	4.72
g-C_3N_4-S_{10}	30.6	53.2	0.671	472	2.63	5.46
g-C_3N_4-S_{20}	32.0	56.8	0.658	483	2.57	7.58
g-C_3N_4-S_{30}	33.9	60.1	0.656	475	2.61	9.55
g-C_3N_4	33.9	60.4	0.648	454	2.73	5.66

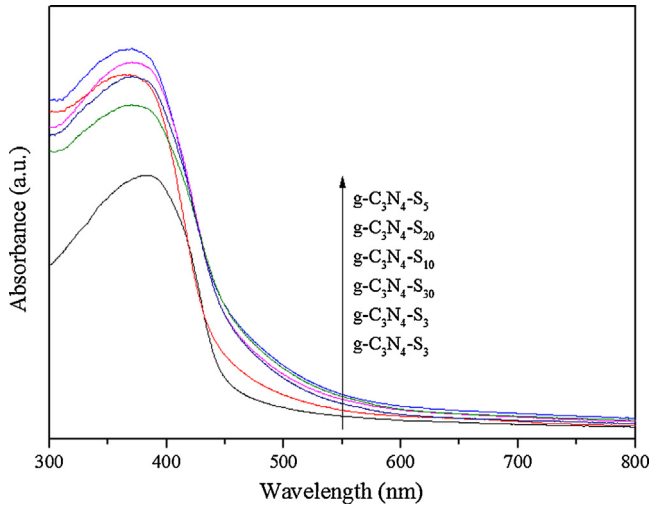

Fig. 5. UV–vis diffuse reflectance spectra of g-C_3N_4-S_x and bulk g-C_3N_4.

3.6. SEM and TEM

The morphologies of samples g-C_3N_4 and g-C_3N_4-S_5 were investigated by scanning transmission microscopy (SEM, Fig. 6a and b) and transmission electron microscopy (TEM, Fig. 6c and d). The particles in both samples exhibit layered and plate-like surface morphologies, as seen in Fig. 6c and d. It is noted that porous structures are only found in g-C_3N_4, g-C_3N_4-S_{30}, and g-C_3N_4-S_{30} (both not shown here), indicating that ammonia is gradually released during the heat treatment [14]. However, there is no porous structure observed in g-C_3N_4-S_5, possibly attributing to the blockage of these pores by sodium species retained. Moreover, particles of g-C_3N_4 are in separate irregular forms but particles of g-C_3N_4-S_5 appear to aggregate to bulk form with small particles surrounded, in Fig. 6a and b. These observations can deduce that $NaNO_3$ involvement might change the morphology of C_3N_4 samples, thus changing the corresponding surface specific areas, as seen in Table 1.

3.7. Photocatalytic measurements

MB was selected as the target pollutant to evaluate the photocatalytic activities of the as-synthesized samples under visible-light

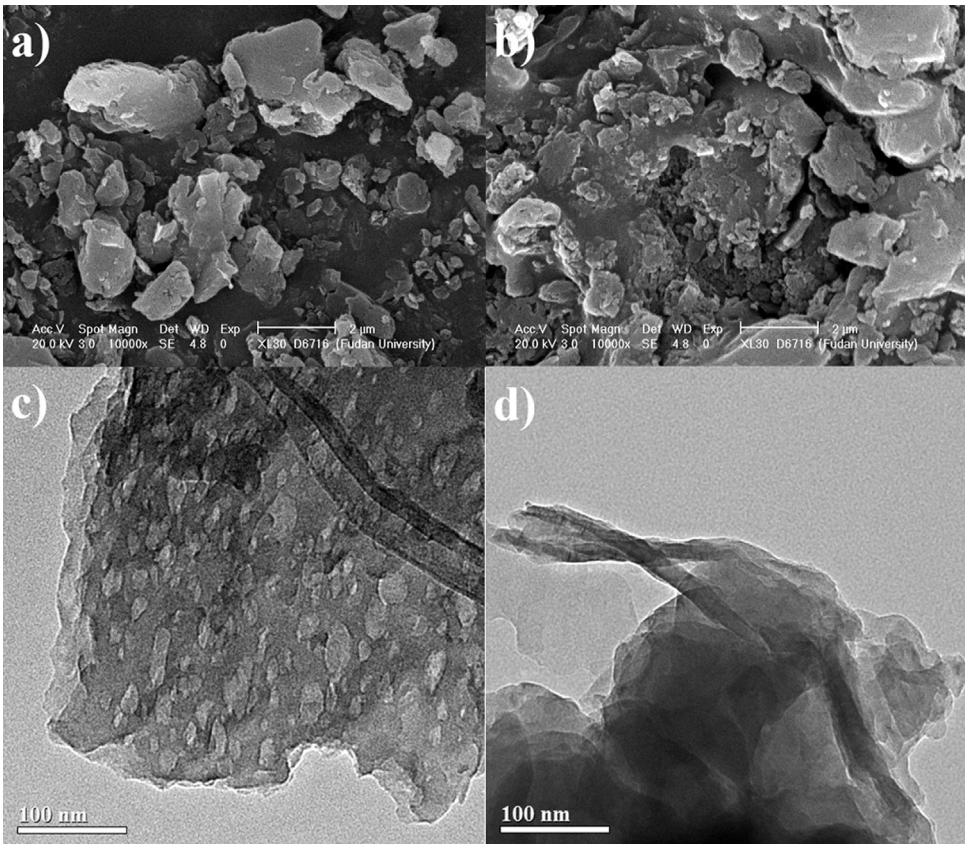

Fig. 6. SEM images of (a) g-C_3N_4 and (b) g-C_3N_4-S_5; TEM images of (c) g-C_3N_4 and (d) g-C_3N_4-S_5.

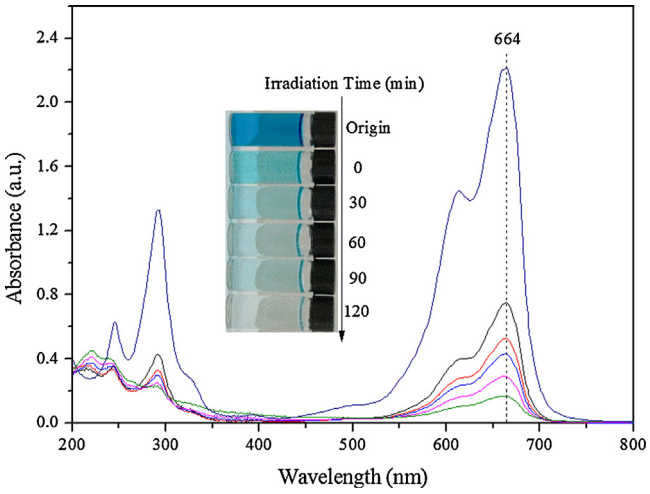

Fig. 7. The temporal evolution of the absorption spectra of the MB solution with g-C_3N_4-S_{10} under visible light irradiation (inset: photo images of degraded MB solutions at different time intervals).

irradiation from a 400 W halide lamp. Fig. 7 shows the temporal evolution of the absorption spectra of the MB solution catalyzed by g-C_3N_4-S_{10}. It was reported that main absorption peak of MB in the presence of g-C_3N_4 were blue shifted from 663 nm to 609 nm during visible light irradiation [35]. However, in our photocatalytic experimental there was no blue shift of main peak of MB observable. As a result, the characteristic absorption peak at 664 nm was employed to evaluate the photocatalytic degradation in this study.

Fig. 8 depicts the variations of MB concentration (C/C_0, C is the concentration of MB at irradiation time t, C_0 is the initial concentration of MB) *versus* irradiation time over as-prepared g-C_3N_4-S_x samples and pure g-C_3N_4. It is evident that direct photolysis of dye MB molecules is negligible in this investigation, as shown in Fig. 8. All g-C_3N_4-S_x samples show stronger adsorption and higher degradation capability than pure g-C_3N_4, especially g-C_3N_4-S_5. Actually, Liu reported that g-C_3N_4 prepared by simple pyrolysis of urea showed good adsorption on MB and no explanation was provided [32]. We could not attribute the stronger adsorption ability of g-C_3N_4-S_5 to physical adsorption because of the similar surface specific areas of g-C_3N_4-S_5 (4.72 g/m^2) to pure g-C_3N_4 (5.66 g/m^2). In addition, we speculated that in our experimental,

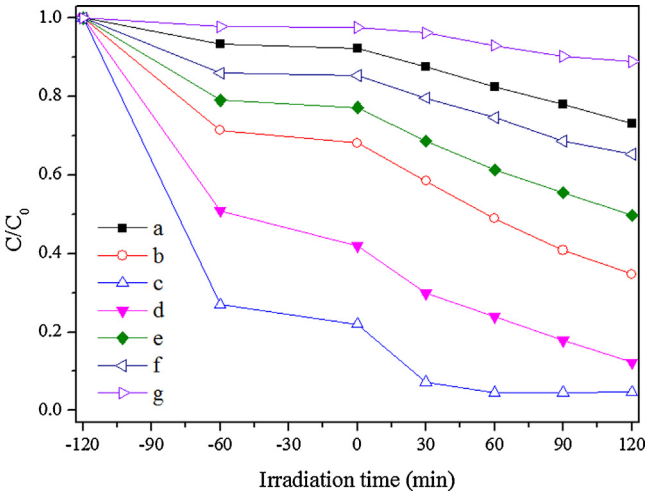

Fig. 8. Photocatalytic degradation of MB over various photocatalysts. (a) g-C_3N_4-S_3; (b) g-C_3N_4-S_5; (c) g-C_3N_4-S_{10}; (d) g-C_3N_4-S_{20}; (e) g-C_3N_4-S_{30}; (f) g-C_3N_4; (g) MB photolysis.

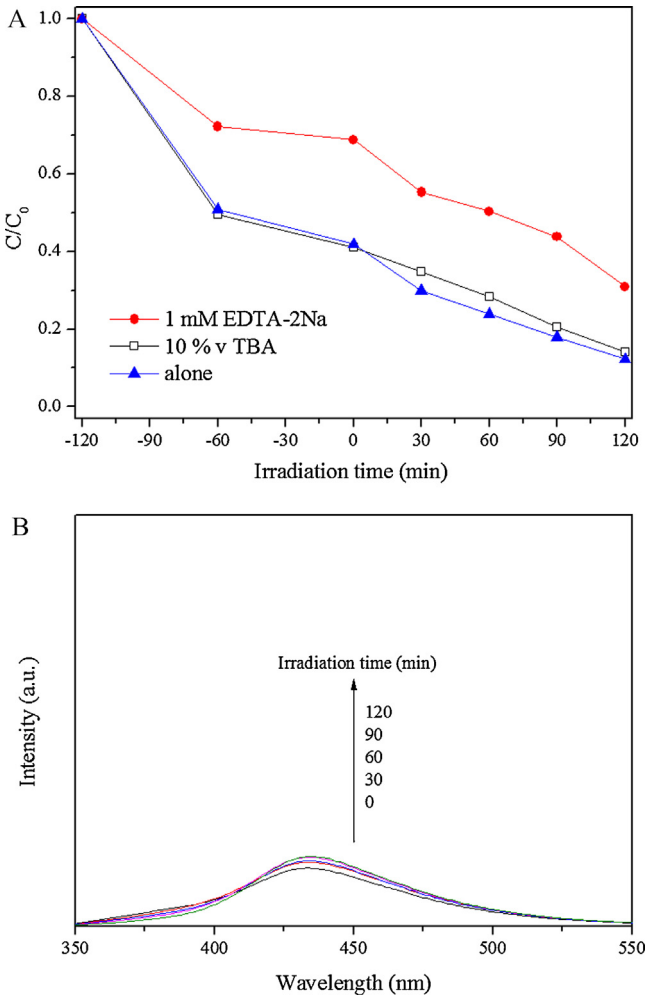

Fig. 9. (A) Comparison of photocatalytic activities for the degradation of MB with or without addition of EDTA-2Na and TBA under visible light irradiation. (B) Fluorescence spectra of TAOH solution generated by g-C_3N_4-S_{10}.

π–π stacking interaction between molecular MB and g-C_3N_4-S_5 was not the main effect since under identical condition no adsorption of MB molecules to pure C_3N_4 was observed at all [36,37]. Finally, we measured the zeta potential values of both g-C_3N_4-S_5 (−37.4 mV) and pure g-C_3N_4 (−18.6 mV) on a zeta potential analyzer *via* dispersing samples into the deionized water. Comparing to pure g-C_3N_4, g-C_3N_4-S_5 surface with more negative charges favored to interact with cationic dye MB molecules, thus favoring adsorption of MB molecules accordingly. As a result, the strong adsorption ability of g-C_3N_4-S_5 on MB was greatly related to the ionization state of catalyst surface. The photocatalytic ability of all samples was in a sequence of g-C_3N_4-S_5 > g-C_3N_4-S_{10} > g-C_3N_4-S_{20} > g-C_3N_4-S_{30} > g-C_3N_4, that was, the g-C_3N_4-S_x with increase of $NaNO_3$ amount showed enhanced adsorption and degradation capability on MB. Among all samples tested, g-C_3N_4-S_5 was the best candidate to remove MB over 95% after only 60 min irradiation. The effect of sodium and potassium species was investigated on the photocatalytic performance of g-C_3N_4 samples, as seen in Fig. A.8. The g-C_3N_4 samples made from same molar ration of melamine to $NaNO_3$ or KNO_3 provide almost same photocatalytic degradation efficiency, revealing that nitrate ions not sodium or potassium species exerted obvious effect on the photocatalytic measurements.

Supplementary material related to this article found, in the online version, at http://dx.doi.org/10.1016/j.apsusc.2013.05.127.

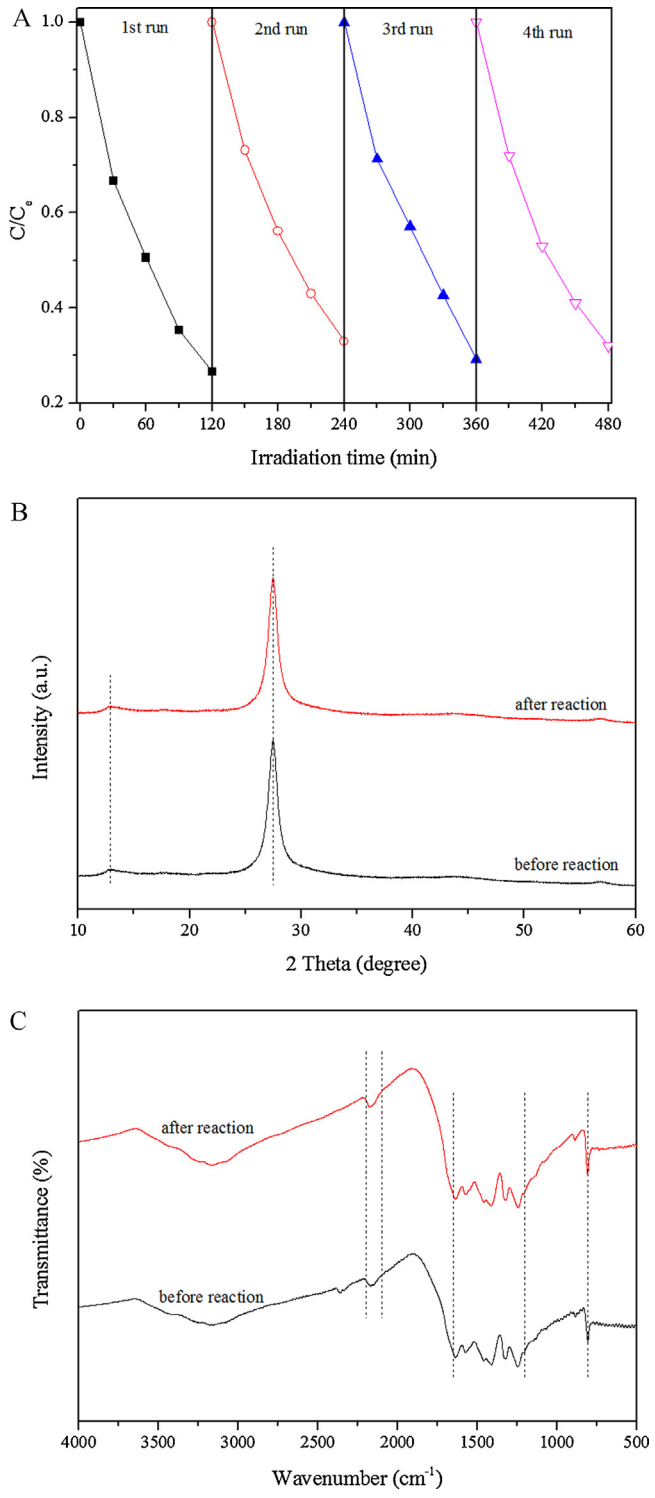

Fig. 10. (A) Cycling runs for the photocatalytic degradation of MB in presence of g-C_3N_4-S_{10} under visible light irradiation. (B) XRD patterns of g-C_3N_4-S_{10} before and after the cycling photocatalytic experiments. (C) FT-IR spectra of g-C_3N_4-S_{10} before and after the cycling photocatalytic experiments.

Photogenerated holes and hydroxyl radicals are two main species for the oxidization of organic molecular in aqueous solution. In order to deep understand the photocatalysis, we investigated the effects of holes and hydroxyl radicals on the photocatalytic evaluation, as shown in Fig. 9A. *tert*-Butyl alcohol (TBA) was selected as a •OH scavenger because it could efficiently entrap the •OH radicals [19]. The addition of TBA caused a small change for the photodegradation of MB, revealing that the hydroxyl radicals were not the main active species. However, the photodegradation efficiency of MB over g-C_3N_4-S_{10} significantly reduced from 70 to 40% after irradiation for 120 min after introducing EDTA-2Na as hole scavengers [38]. These results indicated that the holes played a dominant role in the photodegradation of MB over sample g-C_3N_4-S_{10}. Photoluminescence technique was further employed to detect the hydroxyl radicals formed on the surface of photocatalysts in a semi-quantitative manner by checking the fluorescent intensity of 2-hydroxyterephthalic acid. As shown in Fig. 9B, only slight increase of hydroxyl radicals can be detectable in the photocatalytic system, further implying that the oxidation of MB dye in aqueous solution was not mainly caused by hydroxyl radicals.

The recovery and durability of a given catalyst during a photocatalytic reaction are crucial factors for real industrial applications. Sample g-C_3N_4-S_{10} was selected to operate photocatalysis for four runs through simply centrifugation, washed with ethanol and water for several times, and dried in an oven. There is no obvious decrease of photocatalytic efficiency over MB under visible light irradiation in the recycling reactions, as seen in Fig. 10A. Fig. 10B and C shows XRD and FT-IR patterns of g-C_3N_4-S_{10} before and after 2 h visible light irradiation for the photodegradation of MB. The crytallinity, phase, and chemical structure of g-C_3N_4-S_{10} remained unchanged before and after reactions. Hence, the modified g-C_3N_4 samples were robust and hold an extraordinarily high stability and recyclability. Coupling with the simple preparation and easy recovery, these catalysts may be good alternatives for pollutants treatment and water remediation and will have a potential to real applications in industries.

4. Conclusions

In summary, a facile modification of g-C_3N_4 through co-pyrolysis of melamine and sodium nitrate was conducted in this investigation and the as-synthesized samples were characterized by a collection of techniques, such as XRD, SEM, TEM, UV–vis DRS, nitrogen adsorption, XPS, FT-IR, and element analysis. Based upon structural analysis, we concluded that g-C_3N_4 framework was partially destroyed to produce cyano-containing fragments, which greatly altered the physical and optical properties of g-C_3N_4, further influencing the adsorption and photocatalytic performance of g-C_3N_4 on MB aqueous. The modified g-C_3N_4 samples were robust and able to use at least for four runs without obvious activity loss. In addition, the photocatalysis mechanism was also investigated by entrapping active species.

Acknowledgments

We are grateful to the National Natural Science Foundation of China (Grant numbers 21207089, 41076040, and 20807036), the Innovation Program of Shanghai Municipal Education Commission (Grant number 11YZ113), the project-sponsored by SRF for ROCS, SEM., and Training Program for Young Teachers in Shanghai Colleges and Universities (egd11008) for financial support.

References

[1] T.L. Thompson, J.T. Yates Jr., Surface science studies of the photoactivation of TiO_2 – new photochemical processes, Chemical Reviews 106 (2006) 4428–4453.
[2] M.R. Hoffmann, S.T. Martin, W.Y. Choi, D.W. Bahnemann, Environmental applications of semiconductor photocatalysis, Chemical Reviews 95 (1995) 69–96.
[3] X. Chen, S.S. Mao, Titanium dioxide nanomaterials: synthesis, properties, modifications, and applications, Chemical Reviews 107 (2007) 2891–2959.
[4] P.V. Kamat, TiO_2 nanostructures: recent physical chemistry advances, Journal of Physical Chemistry C 116 (2012) 11849–11851.

[5] M. Shang, W. Wang, S. Sun, L. Zhou, L. Zhang, Bi_2WO_6 nanocrystals with high photocatalytic activities under visible light, Journal of Physical Chemistry C 112 (2008) 10407–10411.
[6] C. Liu, T. Yang, C. Wang, C. Chien, S. Chen, C. Wang, W. Leng, Y. Hwu, H. Lin, Y. Lee, C. Cheng, J. Je, G. Margaritondo, Enhanced photocatalysis, colloidal stability and cytotoxicity of synchrotron X-ray synthesized Au/TiO_2 nanoparticles, Materials Chemistry and Physics 117 (2009) 74–79.
[7] Y. Ao, J. Xu, D. Fu, C. Yuan, A simple method to prepare N-doped titania hollow spheres with high photocatalytic activity under visible light, Journal of Hazardous Materials 167 (2009) 413–417.
[8] Y. Bessekhouad, D. Robert, J.V. Weber, Photocatalytic activity of Cu_2O/TiO_2, Bi_2O_3/TiO_2 and $ZnMn_2O_4/TiO_2$ heterojunctions, Catalysis Today 101 (2005) 315–321.
[9] J. Park, H. Lee, J. Chen, H. Shinokubo, A. Osuka, D. Kim, Photoelectrochemical properties of doubly β-functionalized porphyrin sensitizers for dye-sensitized nanocrystalline-TiO_2 solar cells, Journal of Physical Chemistry C 112 (2008) 16691–16699.
[10] Z. Zou, J. Ye, K. Sayama, H. Arakawa, Direct splitting of water under visible light irradiation with an oxide semiconductor photocatalyst, Nature 414 (2001) 625–627.
[11] I. Tsuji, H. Kato, A. Kudo, Visible-light-induced H_2 evolution from an aqueous solution containing sulfide and sulfite over $ZnS–CuInS_2–AgInS_2$ solid solution photocatalyst, Angewandte Chemie-International Edition 44 (2005) 3565–3568.
[12] X. Wang, K. Maeda, A. Thomas, K. Takanabe, G. Xin, J.M. Carlsson, K. Domen, M. Antonietti, A metal-free polymeric photocatalyst for hydrogen production from water under visible light, Nature Materials 8 (2009) 76–80.
[13] Y. Wang, X. Wang, M. Antonietti, Polymeric graphite carbon nitride as a heterogenous organocatalyst: from photochemistry to multipurpose catalysts in sustainable chemistry, Angewandte Chemie-International Edition 51 (2012) 68–89.
[14] S. Yan, Z. Li, Z. Zou, Photodegradation performance of g-C_3N_4 fabricated by directly heating melamine, Langmuir 25 (2009) 10397–10401.
[15] F. Su, S.C. Mathew, G. Lipner, X. Fu, M. Antonietti, S. Blechert, X. Wang, mpg-C_3N_4-Catalyzed selective oxidation of alcohols using O_2 and visible light, Journal of the American Chemical Society 132 (2010) 16299–16301.
[16] F. Su, M. Antonietti, X. Wang, mpg-C_3N_4 as a solid base catalyst for Knoevenagel condensations and transesterification reactions, Catalysis Science and Technology 2 (2012) 1005–1009.
[17] G. Liu, P. Niu, C. Sun, S.C. Smith, Z. Chen, G. Lu, H. Cheng, Unique electronic structure induced high photoreactivity of sulfur-doped graphitic C_3N_4, Journal of the American Chemical Society 132 (2010) 11642–11648.
[18] X. Wang, X. Chen, A. Thomas, X. Fu, M. Antonietti, Metal-containing carbon nitride compounds: a new functional organic–metal hybrid material, Advanced Materials 21 (2009) 1609–1612.
[19] S. Yan, Z. Li, Z. Zou, Photodegradation of Rhodamine B and methyl orange over boron-doped g-C_3N_4 under visible light irradiation, Langmuir 26 (2010) 3894–3901.
[20] L. Chen, D. Huang, S. Ren, T. Dong, Y. Chi, G. Chen, Preparation of graphite-like carbon nitride nanoflake film with strong fluorescent and electrochemiluminescent activity, Nanoscale 5 (2013) 225–230.
[21] X. Zhang, X. Xie, H. Wang, J. Zhang, B. Pan, Y. Xie, Enhanced photoresponsive ultrathin graphitic-phase C_3N_4 nanosheets for bioimaging, Journal of the American Chemical Society 135 (2012) 18–21.
[22] P. Niu, L. Zhang, G. Liu, H. Cheng, Graphene-like carbon nitride nanosheets for improved photocatalytic activities, Advanced Functional Materials 22 (2012) 4763–4770.
[23] Y. Zhang, A. Thomas, M. Antonietti, X. Wang, Activation of carbon nitride solids by protonation: morphology changes, enhanced ionic conductivity, and photoconduction experiments, Journal of the American Chemical Society 131 (2009) 50–52.
[24] M.K. Lee, D.S. Kim, S.C. Kim, S.W. Han, I. Kim, D.N. Lee, Effect of NaCl and $CaCl_2$ additives on $NaNO_3$ bath nitriding of steel, Materials Science and Engineering A 527 (2010) 1048–1051.
[25] F. Goettmann, A. Fischer, M. Antonietti, A. Thomas, Chemical synthesis of mesoporous carbon nitrides using hard templates and their use as a metal-free catalyst for Friedel–Crafts reaction of benzene, Angewandte Chemie-International Edition 45 (2006) 4467–4471.
[26] M. Kawaguchi, K. Nozaki, Synthesis, structure, and characteristics of the new host material $[(C_3N_3)_2(NH)_3]_n$, Chemistry of Materials 7 (1995) 257–264.
[27] B. Yue, Q. Li, H. Iwai, T. Kako, J. Ye, Hydrogen production using zinc-doped carbon nitride catalyst irradiated with visible light, Science and Technology of Advanced Materials 12 (2011) 034401.
[28] A. Thomas, A. Fischer, F. Goettmann, M. Antonietti, J.O. Muller, R. Schlogl, J.M. Carlsson, Graphitic carbon nitride materials: variation of structure and morphology and their use as metal-free catalysts, Journal of Materials Chemistry 18 (2008) 4893–4908.
[29] G. Zhang, J. Zhang, M. Zhang, X. Wang, Polycondensation of thiourea into carbon nitride semiconductors as visible light photocatalysts, Journal of Materials Chemistry 22 (2012) 8083–8091.
[30] Q. Guo, Y. Xie, X. Wang, S. Zhang, T. Hou, S. Lv, Synthesis of carbon nitride nanotubes with the C_3N_4 stoichiometry via a benzene-thermal process at low temperatures, Chemical Communications 1 (2004) 26–27.
[31] E.R. Piñero, D.C. Amorós, A.L. Solano, J. Find, U. Wild, R. Schlögl, Structural characterization of N-containing activated carbon fibers prepared from a low softening point petroleum pitch and a melamine resin, Carbon 40 (2002) 597–608.
[32] Y. Cui, J. Zhang, G. Zhang, J. Huang, P. Liu, M. Antonietti, X. Wang, Synthesis of bulk and nanoporous carbon nitride polymers from ammonium thiocyanate for photocatalytic hydrogen evolution, Journal of Materials Chemistry 21 (2011) 13032–13039.
[33] H. Yan, Y. Chen, S. Xu, Synthesis of graphitic carbon nitride by directly heating sulfuric acid treated melamine for enhanced photocatalytic H_2 production from water under visible light, International Journal of Hydrogen Energy 37 (2012) 125–133.
[34] K. Maeda, K. Domen, New non-oxide photocatalysts designed for overall water splitting under visible light, Journal of Physical Chemistry C 111 (2007) 7851–7861.
[35] J. Liu, T. Zhang, Z. Wang, G. Dawson, W. Chen, Simple pyrolysis of urea into graphitic carbon nitride with recyclable adsorption and photocatalytic activity, Journal of Materials Chemistry 21 (2011) 14398–14401.
[36] Y. Wang, R. Shi, J. Lin, Y. Zhu, Enhancement of photocurrent and photocatalytic activity of ZnO hybridized with graphite-like C_3N_4, Energy and Environmental Science 4 (2011) 2922–2929.
[37] H. Zhang, X. Lv, Y. Li, Y. Wang, J. Li, P25-graphene composite as a high performance photocatalyst, ACS Nano 4 (2009) 380–386.
[38] X. Hu, T. Mohamood, W. Ma, C. Chen, J. Zhao, Oxidative decomposition of rhodamine B dye in the presence of VO_2 visible light irradiation: N-deethylation, chromophore cleavage, and mineralization, Journal of Physical Chemistry B 110 (2006) 26012–26018.